ASME Journal of Engineering for Gas Turbines and Power
Online journal at:
https://asmedigitalcollection.asme.org/gasturbinespower

**R. Meloni**[1]
Baker Hughes,
Florence 50127, Italy
e-mail: roberto.meloni@bakerhughes.com

**G. Babazzi**
Baker Hughes,
Florence 50127, Italy

**S. Castellani**
Department of Industrial Engineering,
University of Florence,
Florence 50127, Italy

**G. Lemmi**
Department of Industrial Engineering,
University of Florence,
Florence 50127, Italy

**A. Picchi**
Department of Industrial Engineering,
University of Florence,
Florence 50127, Italy

**S. Galeotti**
Department of Industrial Engineering,
University of Florence,
Florence 50127, Italy

**R. Becchi**
Department of Industrial Engineering,
University of Florence,
Florence 50127, Italy

**A. Andreini**
Department of Industrial Engineering,
University of Florence,
Florence 50127, Italy

# High-Fidelity Simulation for the Lean Blow-Out Analysis of an Industrial Burner Operated With Artificial Exhaust Gas Recirculation

*In this paper an enhanced thickened flame model (TFM) capable of accounting for both premixed and nonpremixed combustion regimes is leveraged to reproduce the extinction limit of an industrial burner operating at atmospheric pressure with a vitiated oxidizer. $CO_2$ is employed to dilute the air, simulating the effects of the exhaust gas recirculation (EGR). The $CO_2$ content in the oxidizer is progressively increased until the occurrence of lean blow-out (LBO). Due to practical constraints, the numerical procedure consists of an acceleration of the experiment trend of $O_2$ depletion. In this context, a dedicated strategy for the dynamic calculation of the laminar properties of the flame—i.e., the laminar flame speed (LFS) and laminar flame thickness (LFT)—as a function of the local elemental mass fraction is used. This quantity evolves during the simulation in response to the time-dependent boundary conditions. It will be demonstrated that the proposed approach is capable of successfully capturing the flame characteristics of both the stable conditions and the transient phase leading to blow-out. In fact, it is found that the adopted combustion model is able to predict the LBO at the same oxidizer composition detected experimentally. Moreover, as extinction is approached, the numerical model reproduces the same dynamics observed during the reactive test. A detailed comparison between the numerical results and experimental measurements during this phase is presented and discussed.* [DOI: 10.1115/1.4070249]

## 1 Introduction

The exhaust gas recirculation (EGR) technology for gas turbine (GT)-based system has not yet found practical applications due to the high installation costs that do not justify the benefits in terms of $NO_x$ reduction; single-digit emissions can be more easily and conveniently achieved through dry low NOx combustors which also offer significantly higher operational flexibility. Additionally, high EGR rates can considerably compromise flame stability, leading to undesired emissions of CO/unburned hydrocarbon [1–3] and even flame extinction. Nevertheless, in recent years, the coupling of EGR with GTs has been gaining increasing interest across various applications—from power generation to mechanical drive installations. In fact, enhancing the combustor's lean blow-out (LBO) resistance can allow for higher EGR rates and, consequently, increased $CO_2$ at the exhaust section of the GT unit. In this way, such technology can pave the way for a more efficient and economically sustainable $CO_2$ capture process. Increasing the carbon dioxide content could not only reduce the total energy consumption of standard amine-based carbon capture units but also enable the adoption of new capture processes, such as those based on adsorption or membrane separation [4].

In this context, the operability window can be enlarged in various ways. The first approach could be the use of microhydrogen injections, whose properties can increase the extinction strain rate of the mixture. Hydrogen can be used as a doping agent in natural gas [5] or as a standalone fuel in pilot lines responsible for flame

Turbo Expo: Turbomachinery Technical Conference & Exposition (GT2025), June 16–20, 2025. GT2025.
[1]Corresponding author.
Manuscript received August 18, 2025; final manuscript received October 10, 2025; published online January 19, 2026. Editor: Jerzy T. Sawicki.

stabilization [6]. The second approach is the optimization of burner and/or combustor design, aiming to minimize unburned hydrocarbon emissions and enhance flame stability by modifying the mixing field and its interaction with burner aerodynamics [7]. In this scenario, computational fluid dynamics (CFD) has become a cornerstone; numerical simulations are increasingly performed to verify and define new concepts and, together with experiments, provide valuable insights into the physics behind flame extinction [8,9].

However, the standard turbulent combustion models usually employed with CFD in industry suffer many limitations when predicting the LBO. Those based on the tabulated chemistry approach (e.g., the flamelet generated manifold (FGM) model) do not pose issues when the set of boundary conditions remains consistent in composition over time. But when flame extinction is driven by oxygen depletion or changes in fuel composition, the predefined chemistry set can no longer adequately describe the phenomena. Furthermore, there are many other reasons that limit their applicability. First, an important limitation of these combustion models is that they cannot accurately account for reactivity based on the actual local composition; at intermediate reaction progress values, the reaction always proceeds based on the tabulated oxidizer compositions. This represents a significant assumption, particularly at high EGR rates, where the reaction is strongly influenced by air vitiation caused by combustion products. Moreover, flame extinction is a complex phenomenon dominated by the interaction of the flame front with local stretch [10]. Very often, the impact of this parameter on the reaction progress source term requires nontrivial customization of the combustion model [11]. Finally, in industrial applications the combustion regime is almost always a mix of premixed and nonpremixed flames; aside from rare exceptions tested only on canonical cases [12], the tabulation is decided a priori and cannot cover both regimes. This is another aspect that tabulated chemistry struggles to capture properly.

This drawback can also be associated with some species transport models, such as the thickened flame model (TFM), whose applicability is theoretically limited to premixed flames. However, its mathematical formulation allows for a higher degree of flexibility and customization. Many works recently published in the literature modify the transport equations of the TFM by leveraging a flame index (FI) to detect the combustion regime, thereby enabling a proper description of nonpremixed combustion as well [6–13]. Another limitation of this model when applied to cases with time-dependent boundary conditions is that the laminar properties required as input must change dynamically. Usually, the laminar flame speed (LFS) and laminar flame thickness (LFT) are imported as polynomial functions of the mixture fraction, but they are calculated for a fixed oxidizer (or fuel) composition.

The present work, while adopting the same strategy described above for nonpremixed combustion modeling with the TFM, proposes a method for the correct calculation of mixture properties based on a tabulation approach. As a validation case, the LBO event of an industrial burner fed with natural gas and operating at increasingly high artificial EGR rates will be presented. The numerical data will be compared with experimental results in order to assess the methodology both near the flame extinction limit and under stable conditions. The ultimate goal of this work is to demonstrate the reliability of the methodology, which, when applied to other design concepts or variants, allows for a further extension of the stability limit against flame loss events.

Section 2 will provide details of the numerical methodology as well as the main features of the experimental setup through which the data were collected.

## 2 Numerical Modeling

**2.1 Multiregime Combustion Model.** The base combustion model on which this study is founded is the TFM [14]. As discussed in the introduction, this combustion model should be used only for the premixed combustion regime. To this end, the Takeno-FI [15] is first defined according to Eq. (1) to discriminate the local (cell-based) combustion regime

$$\mathrm{FI} = \frac{\nabla Y_{\mathrm{F}} \cdot \nabla Y_{\mathrm{ox}}}{|\nabla Y_{\mathrm{F}} \cdot \nabla Y_{\mathrm{ox}}|} \tag{1}$$

In this study, methane is selected as the reference fuel and, obviously, oxygen as the oxidant.

For the premixed regime (FI > 0), the transport equation for the generic species mass fraction $\varphi$ is given by

$$\frac{\partial \bar{\rho}\,\tilde{\varphi}}{\partial t} + \frac{\partial \bar{\rho}\,\tilde{u}_j\,\tilde{\varphi}}{\partial x_j} = \frac{\partial}{\partial x_j}\left(\bar{\rho}\left(EFD_l + (1-\Omega)D_t\right)\frac{\partial \tilde{\varphi}}{\partial x_j}\right) + \frac{E}{F}\dot{\omega}(\tilde{\varphi}) \tag{2}$$

where $E$, $F$, and $\Omega$ represent the efficiency function, the thickening factor, and the flame sensor, respectively. The efficiency function aims to partially recover the decreased turbulence–chemistry interaction caused by the artificially thickened flame front, which filters out part of the flame front wrinkling. It is calculated according to the formulation proposed by Colin et al. [14]. However, a different expression for the dilatation-free velocity at the test filter, $u'_{\Delta_e}$, is used (Eq. (3)) to facilitate its calculation on unstructured grids [16]

$$u'_{\Delta_e} = c\Delta\left|\nabla \times \tilde{\boldsymbol{u}} - \nabla \times \widehat{\tilde{\boldsymbol{u}}}\right| \tag{3}$$

The thickening factor $F$ is expressed in its dynamic formulation, according to the idea published by Wang et al. [17]

$$F = \Omega\,(F_{\max} - 1) + 1 \tag{4}$$

Here, the thickening factor is applied only inside the flame front—as detected by the flame sensor $\Omega$—and is set to unity elsewhere to avoid artificially altering the species diffusivity. Consistently with TFM theory, a unity efficiency function is also set in such regions.

The maximum thickening factor $F_{\max}$ is calculated according to Eq. (5), involving the grid resolution $\Delta x$, the flame thickness, and the number of points, $N$, defined by the user to discretize it

$$F_{\max} = \frac{\Delta x N}{\mathrm{LFT}(\Phi)} \tag{5}$$

Since the laminar flame properties change when the oxidizer composition is modified during the simulation, $N$ can also be dynamically adjusted to prevent excessively high thickening factor values.

The flame sensor $\Omega$ is defined by considering a single reaction as representative of the flame front ($CH_4 + OH <=> CH_3 + H_2O$). This reaction is employed to evaluate both the cell-based and the maximum value in the entire domain of the heat release, as combined in the following equation:

$$\Omega = \tanh\left(\beta \frac{|\overline{\dot{\omega}_i}|}{\max\left(|\overline{\dot{\omega}_i}|\right)}\right) \tag{6}$$

where $\beta$ is a model constant, set to 50 to ensure a rapid transition of the flame sensor to 1 within the flame front.

For the nonpremixed combustion regime (FI < 0), no thickening factor is applied, meaning that Eq. (2) is replaced by the following equation:

$$\frac{\partial \bar{\rho}\,\tilde{\varphi}}{\partial t} + \frac{\partial \bar{\rho}\,\tilde{u}_j\,\tilde{\varphi}}{\partial x_j} = \frac{\partial}{\partial x_j}\left(\bar{\rho}(D_l + D_t)\frac{\partial \tilde{\varphi}}{\partial x_j}\right) + \dot{\omega}(\tilde{\varphi}) \tag{7}$$

This closure implies that a finite rate approach, with no turbulence–chemistry interaction, is employed for the diffusive combustion regime.

A dedicated user-defined function is implemented within the solver of the commercial code ANSYS FLUENT to calculate the main combustion parameters and to handle the finite rate–TFM switch.

**2.2 Calculation of the Laminar Properties for Time-Dependent Boundary Conditions.** As discussed in Sec. 2.1, the TFM requires information about the laminar properties of the flame, which contribute not only to the definition of the thickening factor but also to that of the efficiency function [14]. For problems in which the boundary conditions change during the simulation—as in this work, where the oxidant composition is subjected to progressive oxygen depletion—the determination of these properties is not trivial. When the boundary condition is modified, the flame front does not immediately reflect this change. First, the new information must convectively travel from the inlet across the burner before reaching the flame front (phase 1). Then, a transitional period occurs during which the old and new boundary conditions "mix" (phase 2), before the old condition is eventually fully replaced (phase 3).

In this study, for each phase, the laminar properties are assessed according to the local mixture composition. During the CFD simulation, the cell-based mixture fraction $Z$ (Eq. (8)) is computed using Bilger's formulation [18]

$$Z = \frac{2\left[\frac{Y_C - Y_{C,ox}}{W_C}\right] + \frac{1}{2}\left[\frac{Y_H - Y_{H,ox}}{W_H}\right] - \left[\frac{Y_O - Y_{O,ox}}{W_O}\right]}{2\left[\frac{Y_{C,f} - Y_{C,ox}}{W_C}\right] + \frac{1}{2}\left[\frac{Y_{H,f} - Y_{H,ox}}{W_H}\right] - \left[\frac{Y_{O,f} - Y_{O,ox}}{W_O}\right]} \tag{8}$$

Here, $Y_C$, $Y_H$, and $Y_O$ denote the elemental mass fractions of C, H, and O in the cell, respectively. The subscripts "ox" and "f" refer to the oxidizer and fuel inlets. The elemental mass fraction $Y_i$ $(i = C, H, O)$ is calculated during the simulation from the mass fractions of the $k$th species as follows:

$$Y_i = \sum_k a_{i,k} Y_k \frac{W_i}{W_k} \tag{9}$$

where $a_{i,k}$ is the number of atoms of element $i$ contained in species $k$. In this study, a skeletal mechanism comprising 19 species and 62 reactions is used [6]. The computed mixture fraction $Z$ is then used as an independent variable to interpolate polynomial curves for the LFS and LFT. These curves are generated from a freely propagating flame in CANTERA [19] using the same chemical mechanism. For each oxidizer composition, a set of polynomial curves is stored in the user-defined function.

It is worth noting that the boundary conditions are modified through two distinct step changes in the oxidizer inlet composition. Starting from pure air, the first step involves $CO_2$ vitiation, reducing the oxygen concentration to 18.6% by volume. In the second step, an additional increase in $CO_2$ further lowers the oxygen concentration to 16.2% by volume.

The exact moment at which Eq. (8) is updated to reflect a change in the boundary conditions is determined as follows. Each time the oxidizer composition is changed, a new passive scalar is injected from the inlet while the passive scalar associated with the previous composition is turned off. This procedure ensures proper tracking of each oxidizer stream within the computational domain. When the ratio of the volume averages of the new to the old scalar reaches approximately 0.5 in the flame zone, the mixture fraction equation is updated. This procedure guarantees a reasonably smooth, though not perfect, transition in the calculation of the laminar flame properties. After the change is implemented, the simulation is run for at least 5 flow through times (FTTs) of the combustor to allow a new steady-state to be reached with the new oxidizer.

It is important to note that the procedure described above affects only the premixed portion of the combustion model; the non-premixed regime remains entirely unaffected. This should have only a minimal impact on the simulated design under the selected test conditions at high oxygen levels, since the flame is primarily stabilized by pilot flames characterized by a nonpremixed regime. However, when the oxygen content is decreased, the lifting of the flame from the pilots promotes mixing, and the premixed regime becomes dominant. In Sec. 4, it will be demonstrated that the LBO occurs long after the modification of the boundary condition—indicating that, despite its imperfections, the procedure does not significantly impact the overall behavior of the flame.

**2.3 Computational Grid and Numerical Settings.** More than in other combustion models, the computational grid plays a crucial role in the proposed methodology. In the premixed regime, the spatial resolution must allow the TFM to capture the species profiles within the thermal thickness. Conversely, in the nonpremixed regime, the mesh resolution should be fine enough to accurately describe mixing among the reactants and capture the effect of strain rate on the heat release rate (HRR).

Figure 1 shows the static grid designed for this study, which remains unchanged across all operating conditions. No special refinement is applied in the oxidizer plenum, while a resolution of 600 $\mu$m is adopted inside the burner and for the first 15 burner-exit-diameters of the combustion chamber. This conservative choice is driven by the significant lift-off observed experimentally when the flame operates with a high percentage of artificial EGR. Additional local mesh refinement is applied in the pilot fuel line channels and within the primary zone, where fuel is injected through multiple equally spaced holes around the burner tip. In these regions, the mesh resolution is set to 200 $\mu$m, primarily to capture the initial phase when the combustor operates with air. These resolutions are determined based on the expected combustion regime at key locations of the combustor under different oxidizer compositions, while keeping the total mesh count under control (resulting in approximately $30 \times 10^6$ polyhedral elements).

When operating with air, the flame is expected to anchor immediately downstream of the burner tip, burning primarily in a

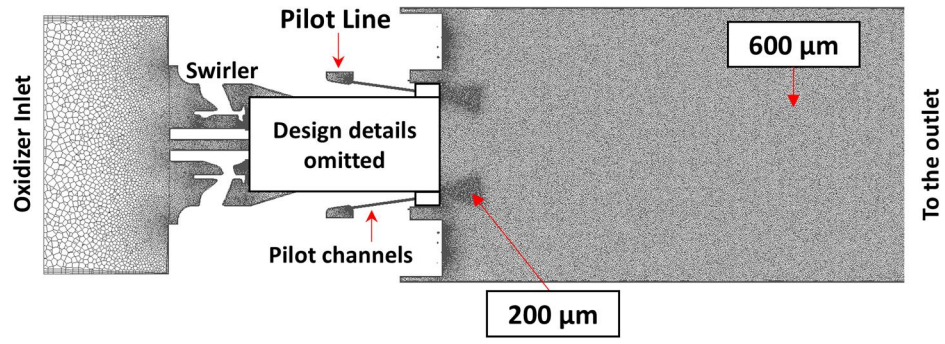


**Fig. 1 Computational grid visualized along the longitudinal midplane, highlighting the different mesh resolutions**

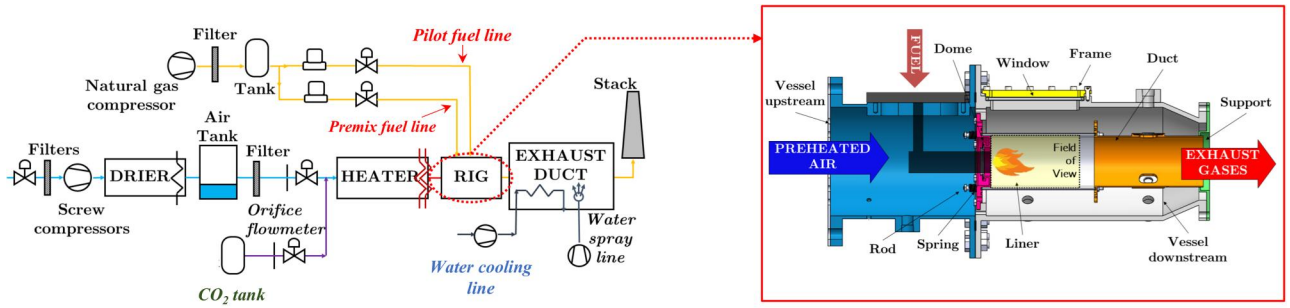


**Fig. 2 Test article scheme (*a*) and detailed view of the combustion arrangement (*b*)**

diffusive mode. As demonstrated in Ref. [20], a 200 $\mu$m resolution is sufficient for a satisfactory prediction of the global HRR distribution within the scope of this analysis. Even in the worst-case scenario of a stoichiometric premixed mixture, where the LFT is approximately 350 $\mu$m, both implemented mesh resolutions enable proper TFM functioning.

Under high EGR conditions, the flame is expected to be highly lifted, with the nonpremixed regime playing a marginal impact. At stoichiometric conditions, the premixed LFT is approximately 900 $\mu$m, and both grid resolutions are adequate for discretizing the flame front.

Concerning the boundary conditions, mass flow rates are prescribed at the oxidizer and fuel inlets, while a pressure outlet is set at the combustor exit (not shown in Fig. 1). For the thermal boundary conditions of the flame tube walls, heat loss is modeled using a heat transfer coefficient of 35 W/m$^2$ K and the bulk oxidizer temperature. The discrete ordinates radiation model is employed, with semi-transparent boundaries for quartz and an optically thick gas model.

For the numerical settings, an incompressible pressure-based solver is used, with the wall-adapting local eddy viscosity [21] model for subgrid-scale turbulence closure in large eddy simulation. All transport equations are discretized at second order, with implicit bounded time-step advancement. The time-step is set to maintain a Courant–Friedrichs–Lewy number below 3 throughout the simulation. A total of 18 FTTs are simulated: five for each of the first two steps and eight for the final step, capturing the transition from stable conditions to blowout.

## 3 Test Rig and Numerical Conditions

The test campaign from which the selected LBO trend is retrieved was conducted at the Technology for High Temperature Lab of the University of Florence. A schematic of the test article is shown in Fig. 2(*a*). The facility is capable of operating with up to 1 kg/s of oxidizer, which can range from pure air to a blend of air and inert gases ($CO_2$, $N_2$, etc.) to achieve a desired oxygen level. The use of $CO_2$-vitiated air to simulate EGR in this study is due to storage limitations of the experimental facility. Nevertheless, since $CO_2$ dilution represents a more severe condition in terms of combustion stability, the findings remain fully representative and valid even if the same design is operated with actual EGR [22,23]. The maximum oxidizer temperature is set to 400 °C using a 600-kW electric heater. The mixture is always heated downstream of the oxidizer stream inlets to ensure complete mixing. The preheated oxidizer is then split into three main streams: the first supplies the premixer, the second feeds the effusion-cooled dome, and the third cools the quartz by external convection. The mass flow distribution among these three streams is determined through a flow network model, based on the effective area of each component.

Regarding fuel injection, the facility allows for a maximum of three independent fuel lines, enabling multigas operation [6]. However, in the present study, only the pilot fuel line is used, despite the burner also having a premixed line.

Figure 2(*b*) provides a detailed view of the combustion system. The casing includes two perpendicular windows, allowing flame visualization through the quartz. High-resolution imaging is employed for particle image velocimetry and flame chemiluminescence measurements. Flame images are captured using a Phantom MIRO M340 camera coupled with an intensifier.

A bandpass filter for OH* (or CH* for hydrocarbon-based fuels) can be used to characterize the flame morphology. Typically, data acquisition is performed at a sampling frequency of 1000 Hz, with an exposure time of 0.5 ms and a constant gain across all operating conditions.

The test rig is also equipped with a HORIBA PG300 for emissions characterization. The gas is sampled at the end of the metallic liner, located downstream of the quartz section, and is maintained at approximately 150 °C to prevent condensation. At roughly the same axial location, a dynamic pressure transducer is installed to monitor acoustic pressure pulsations inside the flame tube.

Table 1 summarizes the main test rig parameters. The oxidizer temperature is maintained at approximately 573 K, and the operating pressure is atmospheric. The fuel composition includes a small fraction of ethane and inert gases, which are not considered in the CFD simulations, where pure methane is used instead. This choice is not expected to significantly affect the behavior of the numerical model while allowing a substantial reduction in computational cost, as the inclusion of ethane chemistry in the skeletal mechanism would be impractical. The fuel mass flow rate remains constant throughout the LBO test, while the addition of $CO_2$ leads to a slight decrease in adiabatic flame temperature.

**Table 1 Test conditions considered for the simulation**

| Parameter | Value |
|---|---|
| Oxidizer temperature | 573 K |
| Oxidizer composition range | From pure air to 16% $O_2$ vol. |
| Oxidizer total mass flow rate | 320 g/s |
| Fuel composition | 96% $CH_4$, 3% $C_2H_6$, 1% inert |
| Fuel temperature | 323 K |
| Pilot split | 100% |
| Operating pressure | 1.016 bar |
| Thermal power | 75 kW |

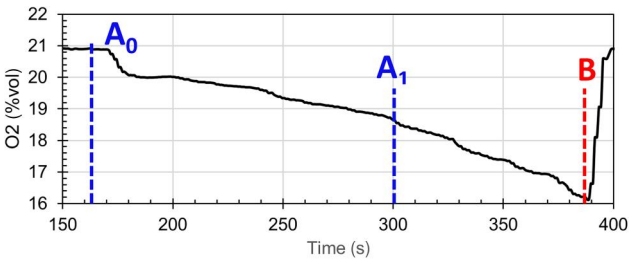


**Fig. 3 Experimental trend of the oxygen content during the LBO test. The vertical lines identify the conditions used in the numerical simulation.**

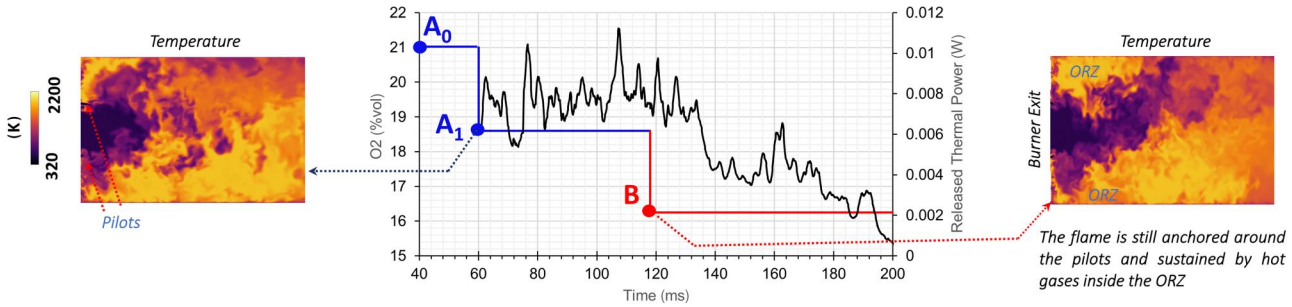


**Fig. 4 Numerical trend of the oxygen content reduction (left *Y*-axis) and instantaneous heat release (right *Y*-axis). The temperature contours correspond to the end of the run with pure air (left) and the end of the run with the first $O_2$ depletion (right).**

## 4 Results and Discussion

Experimentally, the LBO limit is determined by gradually increasing the $CO_2$ content through several small steps. Figure 3 illustrates the decrease in $O_2$ concentration in the oxidizer over the four minutes required for flame extinction. In the numerical investigation, a discrete number of oxygen reduction steps must be considered to minimize computational effort. In Fig. 3, the three vertical dashed lines indicate the oxygen levels implemented in the CFD simulation: the first ($A_0$) corresponds to pure air as the oxidizer, the second ($A_1$) is simulated with $X_{O2} = 18.6\%$, while the last one ($B$) corresponds to $X_{O2} = 16.2\%$.

**4.1 Numerical Versus Experimental Trends Toward Lean Blow-Out.** The simulated physical time for the first two steps ($A_0$ and $A_1$) is set to approximately 60 ms each, corresponding to about 5 FTTs of the combustor. Once $CO_2$ is injected into the domain, it takes around 5 ms to reach the primary zone from the inlet. Therefore, 60 ms is more than sufficient to assess the system's behavior following the boundary condition change and allow the simulation to reach a new steady-state condition.

The mass-averaged heat release trend inside the combustor is shown in Fig. 4 and correlated with the oxidizer composition. After the first oxygen reduction, the heat release undergoes a slight decrease (around 70 ms) but subsequently recovers to its initial value. The same figure also presents instantaneous temperature contour plots on the longitudinal plane at the beginning (left) and end (right) of the first $O_2$ depletion. A comparison of these maps suggests that the flame maintains its structure when transitioning from pure air to $CO_2$-diluted air as the oxidizer. The outer recirculation zones (ORZs), located at the corners between the quartz and the dome plate and generated by the swirled flow, exhibit temperatures close to the peak values, sustaining pilot oxidation through radical interactions. This demonstrates that burner operability remains uncompromised at this level of oxygen reduction. Nevertheless, the effects of increased $CO_2$ in the oxidizer are observable in terms of both CO emissions, measured at the outlet section, and pressure fluctuations. Regarding CO, Fig. 5(*a*) compares the numerical trend with experimental data. Relative to the emission levels recorded when operating with air, the first increase in $CO_2$ results in a fourfold rise in CO. As highlighted by Galeotti et al. [24], this behavior appears to be primarily driven by chemical equilibrium effects, with thermal effects being almost negligible. Numerically, CO is slightly underpredicted (−10%) when using air as oxidizer, while the impact of $CO_2$ addition is overestimated. However, given the challenges associated with CO prediction, the model satisfactorily captures the system's response to $CO_2$ dilution.

Figure 5(*b*) presents the fast Fourier transforms of the experimental and numerical acoustic pressure signals. Experimentally, only broadband noise is observed when operating with air, whereas the introduction of $CO_2$ induces a mild instability with a peak near 300 Hz. The numerical model reproduces the same frequency but also exhibits two additional peaks at 150 Hz and 470 Hz, which are not observed in the experiments. These peaks appear to be the lower and upper harmonics of the 300 Hz mode, respectively. This result suggests that the numerical model predicts a higher level of instability compared to the experiment.

Returning to Fig. 4, and specifically to the events following the second change in oxidizer composition (point B), the heat release trend exhibits a noticeable decline in combustor reactivity after approximately 15 ms. Subsequently, the flame takes a relatively long time to extinguish, as the heat release undergoes intermittent local peaks, such as those observed at 146 ms, 156 ms, and 163 ms. This transient phase is followed by a further reduction in reactivity, ultimately leading to complete LBO at 200 ms. The Sec. 4.2 will provide a detailed analysis of this transient phase leading to flame extinction. However, it is important to highlight a key observation: the fact that the flame extinguishes 80 ms after the second change in boundary conditions suggests that the overall system behavior is

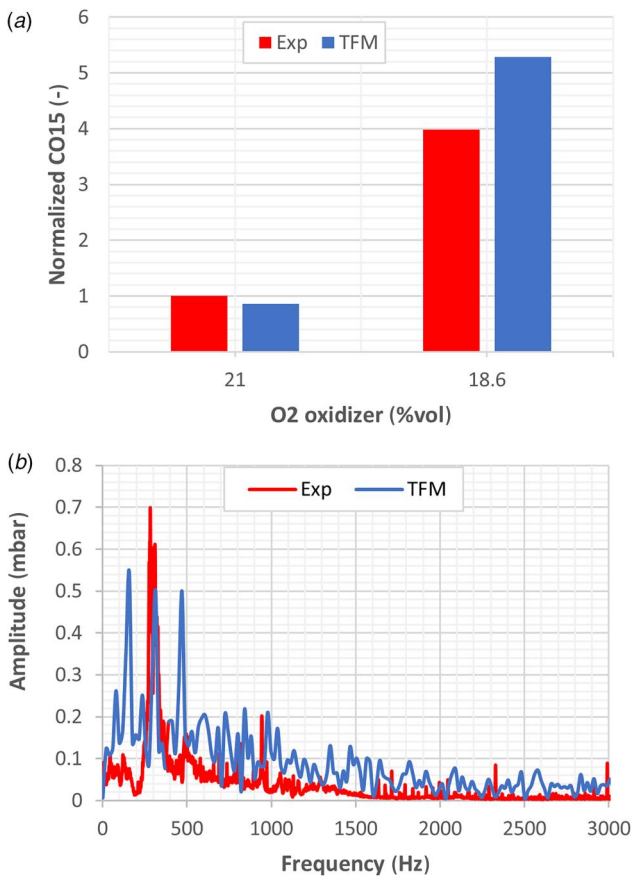


**Fig. 5 (*a*) CO emission and (*b*) fast Fourier transform analysis of the acoustic pressure signals (experimental and numerical results) inside the combustor**

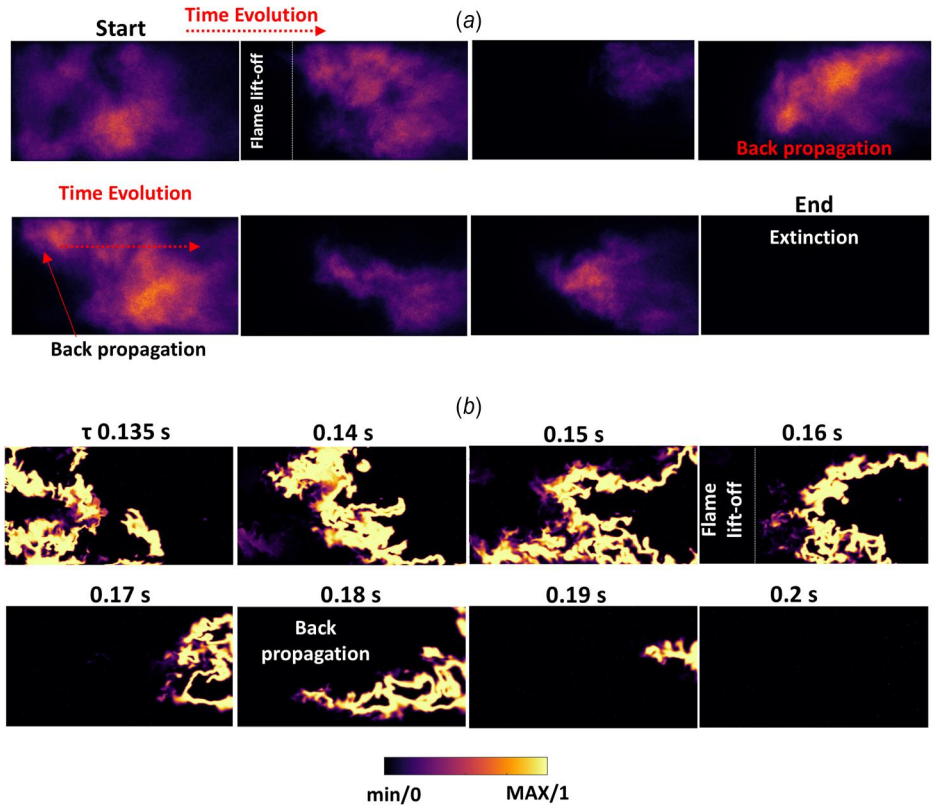


**Fig. 6 (*a*) Normalized experimental line of sight OH and (*b*) numerical Ω sensor on the domain midplane**

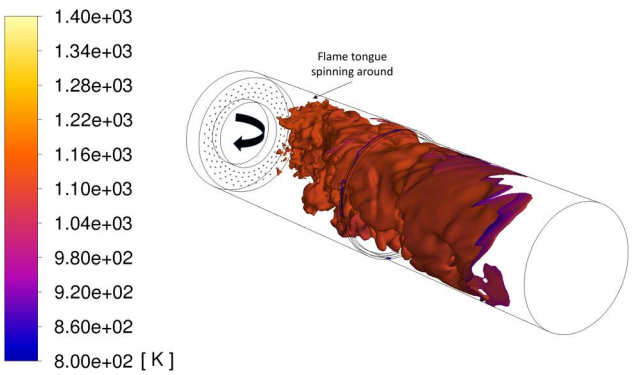


**Fig. 7 Flame front assuming a tongue shape during the LBO phase ($O_2 = 16.2\%$). The iso-progress variable surface is characterized by the instantaneous temperature field.**

unlikely to be significantly influenced by the numerical strategy outlined in Sec. 2.2.

**4.2 Analysis of the Flame-Out Mechanism.** A qualitative comparison between experimental observations and numerical results is presented in Fig. 6, where the instantaneous OH* chemiluminescence contours (experiments) and the flame sensor Ω (CFD) are shown during the flame-loss phase. Numerically, the snapshots correspond to $\tau > 135$ ms, when the flame begins to suffer from oxygen depletion following the second boundary condition change. Experimentally, the images capture the last 3.5 s before flame extinction.

During the tests (Fig. 6(*a*)), the flame periodically undergoes an increase in lift-off height, followed by backpropagation events that promote reattachment of OH* toward the pilot jets. This backpropagation occurs through localized flame structures rather than uniformly across the section. The process repeats several times until the heat release zone moves too far from the pilots and is ultimately pushed out of the combustor.

The CFD simulation exhibits the same behavior: at 150 ms and 180 ms, the flame propagates toward the burner following lift-off events at 140 ms and 160 ms, respectively. Examining the numerical solution at one of these time frames provides insight into the nature of the isolated structures observed in the chemiluminescence images. The flame adopts a "tongue" shape that, influenced by the swirled flow, rotates circumferentially around the flame tube. This structure is visualized in Fig. 7 using an isoprogress variable surface, defined as the sum of the CO and $CO_2$ mass fractions, with a threshold value of 0.5 identifying the flame front. The backpropagation mechanism, which influences the lift-off height, is thus linked to the axial movement of the flame tongue. This fluctuation is driven by the interaction between radicals and the velocity field within the primary zone, particularly inside the ORZs.

Figure 8 overlays velocity vectors and OH radical concentration in the primary zone during a backpropagation event. The first snapshot serves as a reference for a stable flame: in this condition, radicals sustain fuel oxidation due to their high concentration within the ORZs, especially in localized stagnation vortices. Focusing on the backpropagation dynamics, in frame 1 (upper section), OH radicals are initially trapped in recirculating structures near the pilot jet, aiding flame stabilization. However, after 1 ms (frame 2), this region is entirely quenched, likely due to an increase in local strain rate or heat loss, reducing reactivity, as discussed in Ref. [8]. In frame 3, the flame stabilizes within a newly formed vortex (magnified view), illustrating that backpropagation results from the interaction between radicals and local flow structures. The same findings apply to the inner recirculation zone (bottom part of the figures), where a similar interaction between flow structures and radical concentration governs flame dynamics.

**4.3 Dynamic Behavior Analysis During Lean Blow-Out.** To gain further insight into the dynamic behavior of the system during

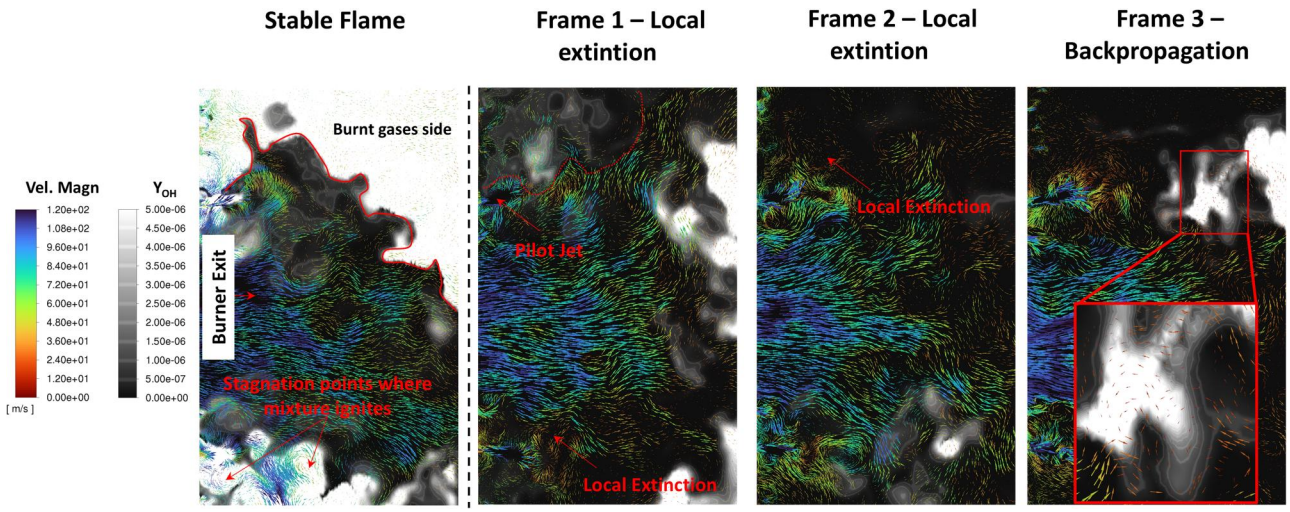


**Fig. 8 Numerical velocity magnitude vectors for stagnation point detection overlapped to the OH mass fraction (gray scale) right downstream of the burner exit**

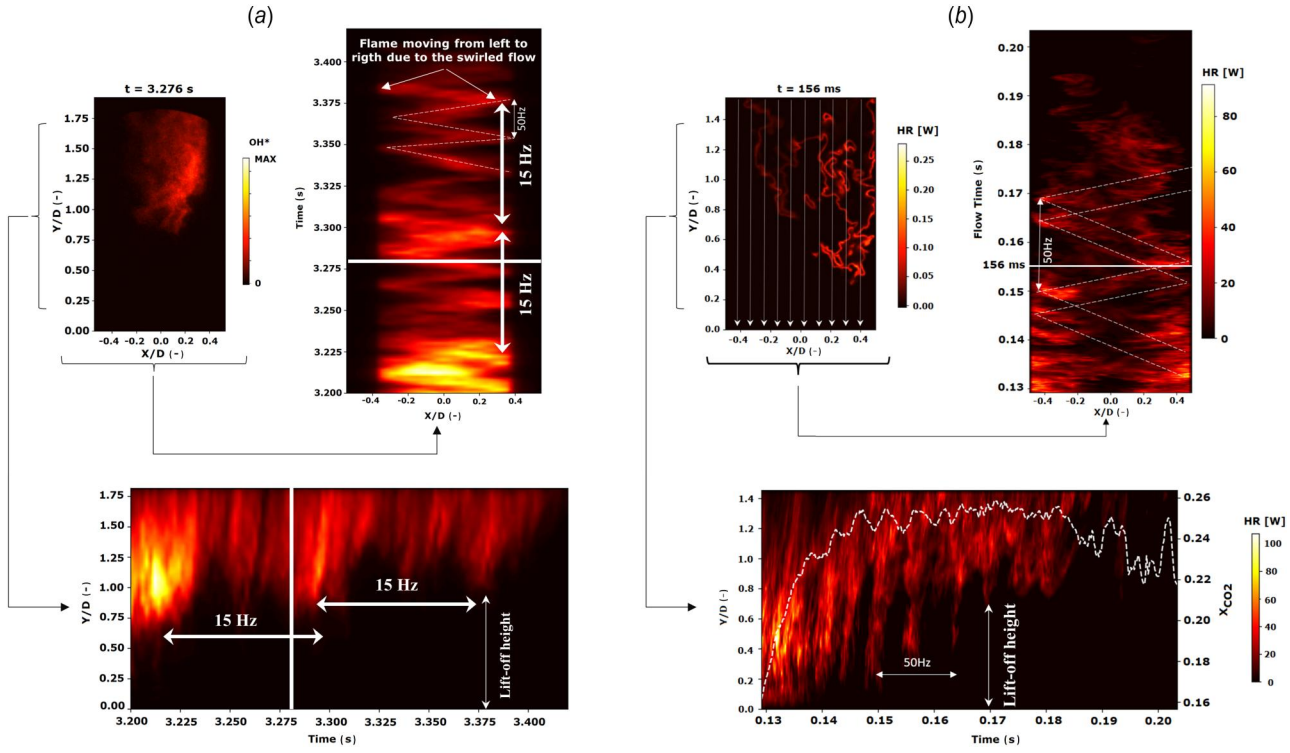


**Fig. 9 Spatial–temporal integration of the OH* intensity for experimental measurements (*a*) and the HRR for the CFD simulation (*b*). Information about low-frequency dynamics and flame lift-off can be retrieved from the *x/D*–Time and *y/D*–Time graphs, respectively.**

the loss of flame, a spatial–temporal integral of the heat release (for the CFD model) and the OH* intensity (for the test) is performed. This calculation sums these quantities along the $x$ ($\forall y$) or $y$ ($\forall x$) direction at each time frame. The formulas are as follows:

$$I(y,t) = \int \dot{\omega}_T(x,y,t)dx \tag{10}$$

$$I(x,t) = \int \dot{\omega}_T(x,y,t)dy \tag{11}$$

The two waterfalls shown in Fig. 9 for both the numerical simulation and the test are the results of this double integration.

Starting with the analysis of the experimental waterfalls, particularly the spatial integration in the $y$-direction (graph $x/D$–Time), a sawtooth structure is clearly visible. This is a result of the flame tongue swirling around the combustor, causing changes in the OH* line-of-sight intensity. The temporal distance between two consecutives OH* peaks at a given $x$-location corresponds to a frequency close to 50 Hz. In the initial part of the analyzed time window (from 3.2 s to 3.225 s), the flame is elongated along the quartz window, leading to high integral values along the $y$-direction. As the flame starts lifting, the portion of the quartz window occupied by the HRR region decreases, lowering the global integral value. Fluctuations in the flame position, related to the backpropagation event, are precisely detected by the changes in OH* intensity over time. After the initial peak, the OH* intensity rises again at around


**Fig. 10 Flame index conditioned by the flame sensor for combustion regime detection**

3.3 s and 3.375 s, with a frequency of around 15 Hz, typical of flame extinction dynamics [8].

The $y/D$–Time graph is crucial for quantifying the flame lift-off height and its variation over time. As expected, this quantity increases closer to flame extinction, with fluctuations due to the backpropagation events, which are also observed in the tests. The 15 Hz frequency of backpropagation is visible in this graph through the temporal distance between local minima of the lift-off height. Regarding the numerical results, the waterfalls show a tone associated with the spinning frequency of the flame at 50 Hz. This frequency is visible not only in the $x/D$–Time graph but also in the $y/D$–Time one. In the latter, backpropagation events are clearly identified by strong variations in lift-off height at this frequency: for a specific $y$-coordinate, the two consecutive HRR traces (e.g., between 0.15 and 0.156 s) correspond to the flame moving from one $x$-location to the opposite $-x$ location. The frequency of this dynamic is determined by the temporal distance between one HRR trace and the next. Unfortunately, the total duration of the numerical simulation is not long enough to capture the 15 Hz dynamics.

In the $y/D$–Time graph, the white curve represents the $CO_2$ mole fraction inside the flame front. This quantity, which differs from the $CO_2$ in the oxidizer by the amount related to fuel combustion, is mainly influenced by the latter. It is notable that the flame lift-off starts to increase when the $CO_2$ curve reaches its maximum value, close to 0.15 s in simulated time. At this point, the 50 Hz tone becomes prominent and persists while the $CO_2$ curve remains flat. After this phase, the flame's reduced reactivity due to flame extinction also causes a drop in $CO_2$.

**4.4 Combustion Regime Analysis.** As discussed in the Sec. 4.3, the flame front undergoes a drastic morphological change as the artificial EGR rate increases. As introduced at the end of Sec. 2.2, this transformation significantly impacts the combustion regime. In this regard, Fig. 10 presents instantaneous contours of the conditioned flame index at two different time frames following each oxygen reduction, approximately at 100 ms and 160 ms, respectively. The conditioned flame index is computed by multiplying the flame index by the omega sensor, ensuring that the analysis is restricted to the actual flame front

$$\mathrm{FI}_c = \mathrm{FI} \cdot \Omega \tag{12}$$

When the flame remains attached to the pilot jets, as shown in Fig. 10(*a*), combustion follows a multiregime process: diffusion combustion dominates near the fuel jets, as expected, while a premixed regime develops further downstream, where fuel and radicals have had sufficient time to mix.

Conversely, as the oxygen content is reduced, the flame transitions to a fully premixed regime. In this case, the fuel injected into the primary zone is not ignited immediately, allowing for a higher degree of mixing before combustion occurs. The snapshot in Fig. 10(*b*) illustrates the flame front near the end of the quartz section, significantly farther from the burner exit. This analysis highlights that the combustion model must account for a multiregime process under the investigated conditions, even when fuel injection occurs entirely through the pilot line.

## 5 Conclusions

In this study, a modified combustion model capable of modulating the chemical source term based on the combustion regime was employed to investigate the LBO event in an industrial burner operating under increasing artificial EGR rates. The adopted strategy for accelerating the transient phase from stable combustion to flame extinction successfully captured the key phenomena governing combustor behavior. Specifically, at high oxygen concentrations in the oxidizer, the model's predictions of CO emissions and pressure fluctuations aligned well with experimental observations. As the system approached flame-out, the CFD simulation reproduced the same flame structure observed in the experiments, characterized by a flame tongue rotating around the combustor at a frequency of 50 Hz.

The numerical model provided valuable insights into the backpropagation events driving the flame from a lifted position toward the burner exit. These events appear to be induced by interactions between flame radicals and localized recirculating zones. Dedicated postprocessing demonstrated that, experimentally, such events are associated with a characteristic frequency of approximately 15 Hz. However, in the simulation, only the dominant 50 Hz frequency linked to the swirled flow was captured, as the simulated transient was not long enough to resolve additional cycles of this dynamic.

This work further highlights the crucial role of a well-established CFD framework in complementing experimental campaigns, providing deeper insights into flame behavior and mixing dynamics that may be challenging to capture experimentally, particularly in the context of multiregime combustion.

## Acknowledgment

The project TRANSITION (fuTure hydRogen Assisted gas turbiNeS for effective carbon capTure IntegratiON) has received funding from the European Union's Horizon Europe research and Innovation programme under Grant Agreement No. 101069665. Views and opinions expressed are however those of the author(s) only and do not necessarily reflect those of the European Union. Neither the European Union nor the granting authority can be held responsible for them.

## Funding Data

- European Union's Horizon Europe research and Innovation programme (Grant Agreement No. 101069665).

## Data Availability Statement

The datasets generated and supporting the findings of this article are obtainable from the corresponding author upon reasonable request.

## Nomenclature

### Latin Letters

$a$ = number of atoms
$D$ = species diffusivity ($m^2/s$)
$E$ = efficiency function

$F$ = thickening factor
$N$ = number of points in flame thickness
$W$ = molecular weight (kg/kmol)
$X$ = mole fraction
$Y$ = mass fraction
$Z$ = mixture fraction

### Greek Symbols

$\nabla$ = gradient operator
$\tau$ = computational time (s)
$\varphi$ = vector of the species mass fractions
$\Phi$ = equivalence ratio
$\Omega$ = flame sensor
$\dot{\omega}$ = reaction rate (kg/(m$^3$ s)

### Subscripts and Superscripts

f = referred to fuel
$i$ = referred to the generic species
$l$ = laminar quantity
max = referred to the thickening factor
ox = referred to oxidant
$t$ = turbulent quantity

### Acronyms

CFD = computational fluid dynamics
EGR = exhaust gas recirculation
FI = flame index
FTT = flow through time
GT = gas turbine
HRR = heat release rate
IRZ = inner recirculation zone
LBO = lean blow-out
LFS = laminar flame speed
LFT = laminar flame thickness
ORZ = outer recirculation zone
TFM = thickened flame model
UC = University of California

## References


[1] ElKady, A. M., Evulet, A., Brand, A., Ursin, T. P., and Lynghjem, A., 2008, "Exhaust Gas Recirculation in DLN F-Class Gas Turbines for Post-Combustion $CO_2$ Capture," ASME Paper No. GT2008-51152.
[2] Evulet, A. T., ELKady, A. M., Branda, A. R., and Chinn, D., 2009, "On the Performance and Operability of GE's Dry Low $NO_x$ Combustors Utilizing Exhaust Gas Recirculation for Post Combustion Carbon Capture," Energy Procedia, **1**(1), pp. 3809–3816.
[3] Babazzi, G., Giannini, N., Meloni, R., Nassini, P. C., Lemmi, G., and Andreini, A., 2023, "On the Impact of the EGR on to the Operability of a Heavy-Duty GT Combustor: A CFD Investigation," 11th European Combustion Meeting, Rouen, France.
[4] Wilberforce, T., Olabi, A. G., Sayed, E. T., Elsaid, K., and Abdelkareem, M. A., 2021, "Progress in Carbon Capture Technologies," Sci. Total Environ., **761**, p. 143203.
[5] Ditaranto, M., Heggset, T., and Berstad, D., 2020, "Concept of Hydrogen Fired Gas Turbine Cycle With Exhaust Gas Recirculation: Assessment of Process Performance," Energy, **192**, p. 116646.
[6] Meloni, R., Babazzi, G., Giannini, N., Castellani, S., Nassini, P. C., Picchi, A., Galeotti, S., Becchi, R., and Andreini, A., 2024, "Thickened Flame Model Extension for Dual Gas GT Combustion: Validation Against Single Cup Atmospheric Test," ASME Paper No. GT2024-122234.
[7] Cerutti, M., Giannini, N., Ceccherini, G., Meloni, R., Matoni, E., Romano, C., and Riccio, G., 2018, "Dry Low $NO_x$ Emissions Operability Enhancement of a Heavy-Duty Gas Turbine by Means of Fuel Burner Design Development and Testing," ASME Paper No. GT2018-76587.
[8] Nassini, P. C., Pampaloni, D., Meloni, R., and Andreini, A., 2021, "Lean Blow-Out Prediction in an Industrial Gas Turbine Combustor Through a LES-Based CFD Analysis," Combust. Flame, **229**, p. 111391.
[9] Cavaliere, D. E., Kariuki, J., and Mastorakos, E., 2013, "A Comparison of the Blow-Off Behavior of Swirl-Stabilized Premixed, Non-Premixed and Spray Flames," Flow Turbul. Combust., **91**(2), pp. 347–372.
[10] Shanbhogue, S. J., Husain, S., and Lieuwen, T., 2009, "Lean Blowoff of Bluff Body Stabilized Flames: Scaling and Dynamics," Prog. Energy Combust. Sci., **35**(1), pp. 98–120.
[11] Meloni, R., Gori, S., Andreini, A., and Nassini, P. C., 2022, "CO Emission Modeling in a Heavy Duty Annular Combustor Operating With Natural Gas," ASME J. Eng. Gas Turbines Power, **144**(1), p. 011011.
[12] Dillon, S., Mercier, R., and Fiorina, B., 2024, "A New Filtered Tabulated Chemistry Model for Multi-Regime Combustion: A Priori Validation on a Laminar Triple Flame," Proc. Combust. Inst., **40**(1–4), p. 105301.
[13] Castellani, S., Meloni, R., Orsino, S., Ansari, N., Yadav, R., Bessette, D., Boxx, I., and Andreini, A., 2023, "High-Fidelity $H_2$–$CH_4$ Jet in Crossflow Modelling With a Flame Index-Controlled Artificially Thickened Flame Model," Int. J. Hydrogen Energy, **48**(90), pp. 35291–35304.
[14] Colin, O., Ducros, F., Veynante, D., and Poinsot, T., 2000, "A Thickened Flame Model for Large Eddy Simulations of Turbulent Premixed Combustion," Phys. Fluids, **12**(7), pp. 1843–1863.
[15] Yamashita, H., Shimada, M., and Takeno, T., 1996, "A Numerical Study on Flame Stability at the Transition Point of Jet Diffusion Flames," Symp. (Int.) Combust., **26**(1), pp. 27–34.
[16] Durand, L., and Polifke, W., 2007, "Implementation of the Thickened Flame Model for Large Eddy Simulation of Turbulent Premixed Combustion in a Commercial Solver," ASME Paper No. GT2007-28188.
[17] Wang, G., Boileau, M., and Veynante, D., 2011, "Implementation of a Dynamic Thickened Flame Model for Large Eddy Simulations of Turbulent Premixed Combustion," Combust. Flame, **158**(11), pp. 2199–2213.
[18] Bilger, R. W., 1977, "Reaction Rates in Diffusion Flames," Combust. Flame, **30**, pp. 277–284.
[19] Goodwin, D. G., Speth, R. L., Moat, H. K., and Weber, B. W., 2018, "Cantera: An Object-Oriented Software Toolkit for Chemical Kinetics, Thermodynamics, and Transport Processes," Zenodo, Geneva, Switzerland.
[20] Lemmi, G., Castellani, S., Nassini, P. C., Picchi, A., Galeotti, S., Becchi, R., Andreini, A., Babazzi, G., and Meloni, R., 2024, "FGM versus ATF: A Comparative LES Analysis in Predicting the Flame Characteristics of an Industrial Lean Premixed Burner for Gas Turbine Applications," Fuel Commun., **19**, p. 100117.
[21] Nicoud, F., and Ducros, F., 1999, "Subgrid-Scale Stress Modelling Based on the Square of the Velocity Gradient Tensor," Flow, Turbul., Combust., **62**(3), pp. 183–200.
[22] Galeotti, S., Picchi, A., Becchi, R., Meloni, R., Babazzi, G., Romano, C., and Andreini, A., 2024, "Experimental Characterization of an Industrial Burner Operated With Simulated EGR," Appl. Therm. Eng., **246**, p. 122943.
[23] Galeotti, S., Picchi, A., Becchi, R., Lemmi, G., Meloni, R., Babazzi, G., Giannini, N., Facchini, B., and Andreini, A., 2024, "Experimental Study on Stability Enhancement of a Natural Gas GT Burner With Hydrogen Flame Piloting Operated With Simulated Exhaust Gas Recirculation," ASME Paper No. GT2024-128732.
[24] Galeotti, S., Picchi, A., Becchi, R., Lemmi, G., Meloni, R., Babazzi, G., Andreini, A., 2025, "Impact of Experimental Strategy to Reproduce EGR in GT Combustor Test Campaigns," 13th Mediterranean Combustion Symposium, Corfù, Greece, June 1–5.